Journal of Hazardous Materials 374 (2019) 319–328

Contents lists available at ScienceDirect

Journal of Hazardous Materials

journal homepage: www.elsevier.com/locate/jhazmat

Highly pure MgO_2 nanoparticles as robust solid oxidant for enhanced Fenton-like degradation of organic contaminants

Doudou Wu[a], Yun Bai[a], Wei Wang[a,*], Hongliang Xia[a], Fatang Tan[a], Shenghua Zhang[b], Bin Su[a], Xinyun Wang[a], Xueliang Qiao[a], Po Keung Wong[c]

[a] State Key Laboratory of Material Processing and Die & Mould Technology, Huazhong University of Science and Technology, Wuhan 430074, Hubei, China
[b] College of Resources and Environmental Science, South-Central University for Nationalities, Wuhan, 430074, Hubei, China
[c] School of Life Sciences, The Chinese University of Hong Kong, Shatin, NT, Hong Kong SAR, China

GRAPHICAL ABSTRACT

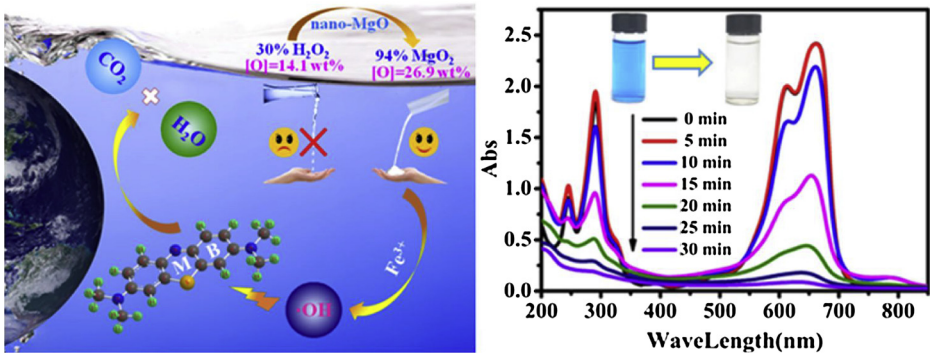

ARTICLE INFO

Keywords:
Magnesium peroxide nanoparticle
Fenton-like reaction
Organic contaminant
Hydroxyl radical

ABSTRACT

In typical Fenton/Fenton-like reactions, H_2O_2 was usually used as an oxidant to degrade organic contaminants. However, liquid H_2O_2 is unstable, easy to decompose and has high biological toxicity especially at high concentration. Herein, highly pure magnesium peroxide (MgO_2) nanoparticles were first synthesized and used instead of H_2O_2 to degrade organic dyes. The structure and morphology of as-prepared products were confirmed by XRD, SEM, TEM and FTIR techniques. The active oxygen content of MgO_2 nanoparticles reached up to 26.93 wt%, suggesting a high purity of the as-prepared sample. The degradation performance of MgO_2 nanoparticles towards organic contaminants was systematically investigated in the terms of the molar ratio of Fe^{3+} to MgO_2, the dosage of MgO_2, initial solution pH and different organic dyes. The results indicated the as-prepared MgO_2 exhibited excellent degradation ability to various types of organic dyes. 10 mg of MgO_2 nanoparticles could almost completely degrade 200 mL of 20 mg/L methylene blue (MB) in 30 min with a TOC removal rate of 70.2%. The efficient degradation performance was ascribed to the generation of hydroxyl radicals in the MgO_2/Fe^{3+} system. The pathways of MB degradation were also proposed based on the determination of the reaction intermediates.

* Corresponding author.
E-mail address: weiwang@hust.edu.cn (W. Wang).

https://doi.org/10.1016/j.jhazmat.2019.04.058
Received 10 January 2019; Received in revised form 15 April 2019; Accepted 16 April 2019
Available online 17 April 2019

1. Introduction

As one of alternative strategies for efficient removal of organic contaminants, advanced oxidation processes (AOPs) have been widely studied for water treatment and soil remediation due to high efficiency, cost-effectiveness and easy handling [1–3]. Among various AOPs, Fenton/Fenton-like reactions have been considered as effective methods to degrade organic wastes, because of the efficient generation of reactive oxygen species (ROS), such as hydroxyl radicals ($^{\cdot}OH$), peroxides (O_2^{2-}) and superoxide anions ($^{\cdot}O_2^-$), resulting from hydrogen peroxide (H_2O_2) [4–6].

However, H_2O_2 as oxidant is highly dependent on suitable reaction environment with extremely acidic pH range (2–4) [7,8]. Furthermore, H_2O_2 is unstable and easy to decompose, which creates problem for transportation and storage. Additionally, the feature of easy decomposition for liquid H_2O_2 will lead to a short lifespan in the oxidation process [9]. Also, it has biological toxicity, causing biofouling in the delivery system especially at high concentration [10]. As early as 1999, H_2O_2 has been classified as a third type of carcinogens by the World Health Organization (WHO) [11]. As a result, alternative oxidants with oxidation capacity similar to H_2O_2 have been employed to overcome these challenges. Solid oxidants [12–16] such as metal peroxides and persulfates are potential substitutes for H_2O_2 in the application of degrading organic pollutions. In recent years, calcium peroxide (CaO_2) [17] and zinc peroxide (ZnO_2) [18] have been widely reported as convenient sources of hydrogen peroxide, oxygen and reactive oxygen species in the field of environmental restoration. Compared with H_2O_2, solid metal peroxides are much stable, convenient for transportation and storage, and can be applied in a wide pH range. The metal peroxides react with water to produce H_2O_2, where M is a divalent metal cation:

$$MO_2 + 2H_2O \rightarrow M(OH)_2 + H_2O_2 \quad (1)$$

Unfortunately, the active oxygen contents of CaO_2 and ZnO_2 are not high, thus a high dosage is required in application. The active oxygen content of commercial CaO_2 is only 16.67 wt%, indicating a low purity. Besides, the theoretical active oxygen contents of CaO_2 and ZnO_2 are 22.22 wt% and 16.49 wt%, respectively, which are much lower than that of MgO_2 (28.57 wt%). In addition, CaO_2 and ZnO_2 react with H_2O to produce $Ca(OH)_2$ and $Zn(OH)_2$, respectively (Eq. (1)). In contrast with $Mg(OH)_2$ (K_{sp} ($Mg(OH)_2 = 1.8 \times 10^{-11}$) generated from MgO_2, the solubility product of $Ca(OH)_2$ (K_{sp} ($Ca(OH)_2 = 5.5 \times 10^{-6}$) is several orders of magnitude higher, which inevitably cause a high leakage of metal ions (Ca^{2+}) and an increase of solution pH, requiring further treatments prior to discharge. As for $Zn(OH)_2$, the leakage of Zn^{2+}, one of heavy metal ions, will cause secondary heavy-metal pollution. Obviously, MgO_2 is better than CaO_2 or ZnO_2 for replacing H_2O_2 used in Fenton/Fenton-like reactions, due to the advantages of non-toxicity, high stability and active oxygen content. As early as 1988, MgO_2 was prepared and mainly used as an antimicrobial agent [19]. However, the reported MgO_2 samples contained the impurities including MgO and $Mg(OH)_2$, resulting in a low purity and active oxygen content [20]. Moreover, the size of prepared MgO_2 particles was usually large, reached several even hundreds of micrometers [21]. To our best knowledge, MgO_2 nanoparticles with high purity (more than 80 wt%) have not been synthesized and used for the degradation of organic contaminants.

Herein, highly pure MgO_2 nanoparticles (> 94 wt%) were synthesized for the first time and used as a substitute for H_2O_2 to degrade organic contaminants (Fig. 1). The as-obtained MgO_2 nanoparticles were characterized by XRD, FTIR, SEM and TEM techniques. The degradation efficiencies of MgO_2 towards organic dyes catalyzed by Fe^{3+} under different conditions were evaluated. The electron spin resonance (ESR) measurements and radical scavenger tests were also conducted to clarify ROS generated in the MgO_2/Fe^{3+} system. On the basis of HPLC-MS analysis, the degradation pathways were also tracked to determine the process of MB degradation.

2. Materials and methods

2.1. Materials

Hydrated ferric sulfate ($Fe_2(SO_4)_3{\cdot}xH_2O$), ferric trichloride hexahydrate ($FeCl_3{\cdot}6H_2O$) and isopropanol (IP) were obtained from Shanghai Chemical Reagent Factory. Magnesium nitrate hexahydrate ($Mg(NO_3)_2{\cdot}6H_2O$), ammonium hydroxide ($NH_3{\cdot}H_2O$), absolute ethyl alcohol (C_2H_5OH), hydrogen peroxide (H_2O_2, 30 wt%), sodium hydroxide (NaOH), sulfuric acid (H_2SO_4, 95.0–98.0 wt%), methylene blue ($C_{16}H_{18}ClN_3S$, MB), methyl orange ($C_{14}H_{14}N_3NaO_3S$, MO) and malachite green ($C_{23}H_{25}N_2Cl$, MG) were purchased from Sinopharm Chemical Reagent Co., Ltd. 5,5-dimethyl-1-pyrroline N-oxide (DMPO, 97 wt%) was provided by Aladdin Chemistry Reagent Chemistry Co., Ltd. All chemicals were of analytical grade and used without further purification.

2.2. Synthesis of MgO_2 nanoparticles

MgO_2 nanoparticles with high purity were synthesized through the reaction between MgO nanoparticles and H_2O_2 for the first time. Firstly, 25.6 g of $Mg(NO_3)_2{\cdot}6H_2O$ was dissolved in 100 mL of distilled water, the solution containing 50 mL of $NH_3{\cdot}H_2O$ and 30 mL of absolute ethyl alcohol was added dropwise to the above mixture under stirring. After constant stirring for another 2 h, the obtained precipitate of $Mg(OH)_2$ was separated by suction filtration from aqueous solution. After washed with distilled water for three time, and then absolute ethyl alcohol for three times, the filtered cake was dried at 80 °C for 12 h in an oven. Then, the dried product was calcined at 450 °C for 2 h at the heating rate of 5 °C/min to yield MgO nanoparticles. Finally, 1.2 g of as-prepared MgO nanoparticles was dispersed in 20 mL of absolute ethyl alcohol and then 20 mL of H_2O_2 (30 wt%) was poured into the suspension. After stirring for 4 h, the solid was separated from the suspension. Subsequently, MgO_2 nanoparticles were obtained after drying at 70 °C for 24 h.

2.3. Characterization of MgO_2 nanoparticles

The X-ray diffraction (XRD) measurements were carried out by a Philips X'Pert Pro X-ray powder diffractometer using Cu K_α radiation (λ = 1.5418 Å) at room temperature. The XRD patterns were recorded in the 2θ range of 10–90°, with a scan speed of 2°/min. Fourier transform infrared (FTIR) spectra were obtained using a Bruker VERTEX 70 spectrometer equipped with a KBr beam splitter (KBr, GR grade) in the wavenumber range of $4000 - 400\ cm^{-1}$. The background spectrum of KBr was also recorded at the same conditions. The elemental composition of the solid residue after the degradation reaction was determined by an Eagle III X-ray fluorescence spectrometer (XRF). The microstructure and morphology observations were conducted using a Nova NanoSEM 450 scanning electron microscope (SEM, acceleration voltage 10 kV, working distance 5 mm) and a Tecnai G2 F30 field emission transmission electron microscope (FTEM, operated at 300 kV) equipped with selected area electron diffraction (SAED) pattern.

2.4. Organic dye degradation experiments

The degradation properties of MgO_2 nanoparticles were evaluated by degradation of organic dyes in aqueous solution (20 mg/L MB, 30 mg/L MO, 80 mg/L MG) at room temperature (Ca. 25 °C). For each experiment, 200 mL of organic dye solution was first added to a glass beaker followed by the addition of 10 mg of MgO_2 nanoparticles under magnetic stirring. After thorough mixing, a certain amount of $Fe_2(SO_4)_3{\cdot}xH_2O$ or $FeCl_3{\cdot}6H_2O$ was added to the mixture to ignite the

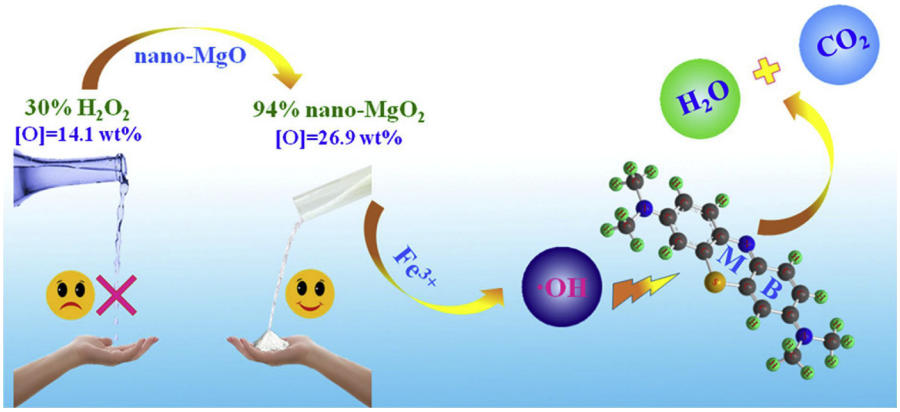

Fig. 1. Schematic illustration of highly pure MgO_2 nanoparticles used instead of H_2O_2 for Fenton-like degradation of organics.

degradation reaction. The initial pH of each experiment was adjusted using NaOH (0.1 M) and H_2SO_4 (0.1 M) to the desired value. At given time intervals, 3 mL of suspension was extracted from the reaction system and filtered immediately by a 0.22 μm-nylon syringe filter to remove any insoluble matter. Then, the concentration of residual dyes in the filtrate was measured by a UV–visible spectrophotometer (UV-670, Shanghai Meipuda Instruments Co., Ltd) to determine the degradation performance of MgO_2 nanoparticles towards organic dyes. The degradation rate was calculated using the decrease in the absorbance of organic dyes at the maximum absorption wavelength, according to Eq. (2).

$$\text{Degradation rate}\ (\%) = \frac{C_0 - C_t}{C_0} \times 100 \quad (2)$$

Where C_0 is the initial concentration of organic dyes, C_t is the concentration of organic dyes at time t.

2.5. Electron spin resonance (ESR) and radical scavenger tests

Electron spin resonance (ESR) spectroscopic experiments were carried out on a JES-FA200 ESR spectrometer (JEOL, Tokyo, Japan) with DMPO as a spin-trapping agent. At given time intervals, about 0.5 mL of aliquot was taken out from the reaction system, and mixed with 10 μL of DMPO immediately. After vibrating for 2 min at room temperature (Ca. 25 °C), a small amount of the mixture was introduced into a capillary for ESR analysis. The parameters for ESR measurements were as follows: modulation frequency of 100 kHz, microwave frequency of 9.15 GHz, microwave power of 3 mW, constant time of 30 ms and sweep time of 30 s. To further support the generation of hydroxyl radical in the MgO_2/Fe^{3+} system, radical scavenger tests were conducted. Isopropanol, a common ·OH scavenger, was added in the MB degradation system to confirm the significant role of ·OH in organic dye degradation.

2.6. HPLC-MS and TOC analysis

To investigate the pathways of organic dye degradation in the MgO_2/Fe^{3+} system, the intermediates originated from MB degradation were characterized by a HPLC-MS (Agilent 1100 LC/MSD Trap XCT) equipped with an Agilent Eclipse XDB-C18 column (150 × 4.6 mm, id, 5 μm particle). The ESI-MS spectra were acquired in a positive ionization mode with an analytical scan range of *m/z* 50–400. The reaction mixtures were injected into the ESI source with a syringe pump at a flow rate of 1 μL/min. Drying gas temperature was set at 280 °C with a flow rate of 10.00 mL/min, and the nebulizing pressure was of 40.00 psi. HV capillary voltage was 3500 V. Total organic carbon (TOC) values were obtained using an Analytic Jena Multi NIC 3100 total organic carbon analyzer. The removal rate of TOC was calculated as follows:

$$\text{Removal rate of TOC}\ (\%) = \frac{C_0 - C_t}{C_0} \times 100 \quad (3)$$

Where C_0 is the initial concentration of TOC of organic dye solution, C_t is the concentration of TOC at degradation time t.

3. Results and discussion

3.1. Structures and morphologies of MgO_2 nanoparticles

Fig. 2a illustrated X-ray diffraction patterns of the as-prepared MgO and MgO_2 nanoparticles. In the XRD pattern of MgO nanoparticles, all the peaks appearing at 2θ = 36.9, 42.9, 62.2, 74.6, 78.5° could be indexed to the (111), (200), (220), (311) and (222) facet of MgO with a periclase structure (JCPDS 78-0430), respectively. No other peaks from impurities were observed, suggesting that the obtained MgO sample did not contain other impurity phases, such as $Mg(OH)_2$, $Mg(NO_3)_2$. It was obvious that the XRD pattern of MgO_2 nanoparticles was far different from that of MgO nanoparticles. There were three broad peaks at 37.1°, 53.5° and 63.7° in the XRD pattern of MgO_2 nanoparticles, corresponding to (200), (220) and (311) of MgO_2 with a cubic structure (JCPDS 76-1363), respectively. No extra diffraction peaks related to Mg $(OH)_2$ or MgO phase were detected, indicating that the prepared MgO_2 sample was highly pure. To quantitatively evaluate the purity of MgO_2 nanoparticles, a titration experiment with 0.02 M $KMnO_4$ were conducted to determine the active oxygen content of MgO_2 nanoparticles. The result showed the active oxygen content was about 26.93 wt%, close to the theoretical value of MgO_2 (28.57 wt%), which was far higher than that of other reported oxidants (Table 1). After calculation, the purity of prepared MgO_2 sample was more than 94 wt%, further manifesting that highly pure MgO_2 was obtained in this work.

FTIR spectra were conducted to determine the functional groups in the as-prepared MgO and MgO_2 nanoparticles. As shown in Fig. 2b, the characteristic absorption peaks of MgO_2 can be observed at 692 cm^{-1} and 866 cm^{-1}, related to the Mg-O [33] and O—O bridge [34] of MgO_2, respectively. Compared with MgO, the intensity of O—O bridge of MgO_2 was stronger than that of MgO and the intensity of Mg-O bridge of MgO_2 was weaker than that of MgO, implying that MgO_2 nanoparticles were successfully synthesized from MgO nanoparticles in this work. As for the peaks appearing at 3441 cm^{-1}, 1637 cm^{-1} and the peak appearing at 1438 cm^{-1}, they were assigned to the adsorbed water and CO_3^{2-} [35,36] on the surface of MgO_2 nanoparticles, respectively.

SEM image of MgO_2 nanoparticles (Fig. 2c) showed that the as-prepared sample exhibited a spherical granular morphology with a diameter of around 40 nm. There was agglomeration between particles, due to a high surface energy of nanoparticles. The inset of magnified image in the TEM image (the top-left inset of Fig. 2d) clearly

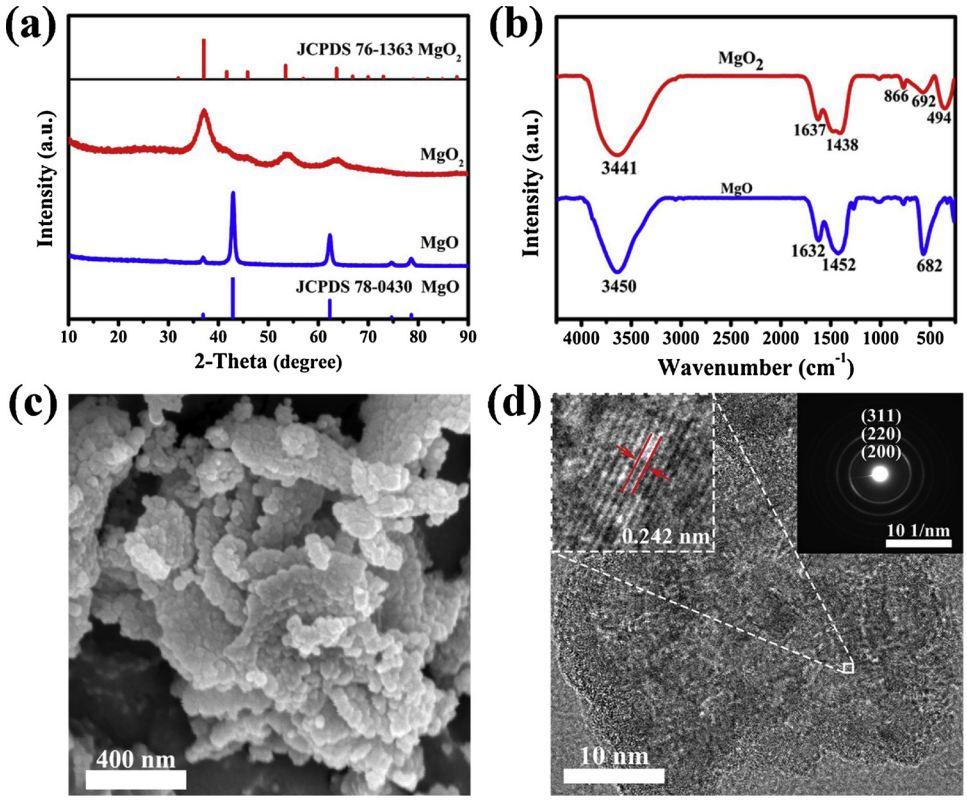

Fig. 2. XRD patterns (a), FTIR spectra (b) of MgO and MgO_2 nanoparticles, SEM image (c), HRTEM and SAED image (inset) (d) of MgO_2 nanoparticles.

Table 1
Comparison of the purities and active oxygen contents of various oxidants.

Oxidant	Molecular formula	Purity (wt%)	Active oxygen Content (wt %)	Reference
Magnesium peroxide	MgO_2	94.26	26.93	This work
		11.6	3.3	[22]
		24–28	6.9-8	[23]
		~70	~20	[24]
Calcium peroxide	CaO_2	70	15.6	[25]
Zinc peroxide	ZnO_2	73-80	12-13	[24]
		97	16	[26]
Barium peroxide	BaO_2	95	9	[27]
Hydrogen peroxide	H_2O_2	30	14.1	[28]
Potassium persulfate	$K_2S_2O_8$	99.5	5.9	[29]
Sodium persulfate	$Na_2S_2O_8$	99	6.7	[30]
Ammonium persulfate	$(NH_4)_2S_2O_8$	98	6.9	[31]
Sodium percarbonate	$Na_2CO_3{\cdot}1.5H_2O_2$	98	15.1	[32]

demonstrated the lattice fringe with an interplanar spacing of 0.242 nm, related to the (200) plane of MgO_2. The SAED pattern (the top-right inset of Fig. 2d) showed several bright-circled rings, indicating that the as-prepared MgO_2 nanoparticles were in polycrystalline state. Moreover, the most intensive three diffraction rings corresponded to the (200), (220) and (311) planes of MgO_2, respectively, which was in accordance with the result of XRD analysis.

3.2. Organic dye degradation in the MgO_2/Fe^{3+} system

In order to investigate the effect of Fe^{3+} dosage on the performance of MB degradation in the MgO_2/Fe^{3+} system, a batch of experiments were conducted in the presence of MgO_2 (10 mg) and MB (200 mL, 20 mg/L) with different molar ratio of Fe^{3+} to MgO_2 from 0:1 to 0.8:1. As shown in Fig. 3a, Fe^{3+} played an effective catalytic role in the MgO_2/Fe^{3+} degradation system. If without Fe^{3+}, MB could not be nearly degraded by MgO_2 nanoparticles alone. As the amount of Fe^{3+} increased, the degradation performance was significantly improved. This improvement could be ascribed to the generation of more ROS when more Fe^{3+} was added as a catalyst to this Fenton-like reaction system. When the ratio of Fe^{3+} to MgO_2 is 0.7:1, the MB solution could be almost degraded completely in 30 min. Since then, increasing the amount of Fe^{3+} had slight effect on improving the degradation performance of MB. It was noteworthy that MB was hardly degraded in the first 5 min for each degradation reaction, which was different from the conventional Fenton/Fenton-like reactions using H_2O_2 as an oxidant. This phenomenon can be explained by the slow release of MgO_2 rather than the rapid decomposition like H_2O_2.

As an effective oxidant, the amount of MgO_2 had also been explored for its effect on the degradation of MB under the condition where the ratio of Fe^{3+} to MgO_2 was always kept at 0.7:1. In Fig. 3b, the degradation rate of MB increased sharply as the dosage of MgO_2 increased from 0 to 12 mg. If without any addition of MgO_2 nanoparticles, no significant change was observed in the concentration of MB, indicating that MgO_2 was an essential component in the MgO_2/Fe^{3+} system for MB degradation. When 5 mg of MgO_2 was used, the degradation rate of MB was less than 60% in 60 min. While the MB solution could be almost degraded completely by 10 mg of MgO_2 in 30 min. Thereafter, further increasing the dosage of MgO_2 could only slightly improve the rate of MB degradation. The result presented above can be explained as follows. With increasing the dosage of MgO_2, more H_2O_2 will be slowly generated via Eq. (4) (Fig. S1a and S1b), resulting in the generation of more ROS in a short time. Therefore, the degradation ability of the MgO_2/Fe^{3+} system can be highly enhanced with more addition of MgO_2.

$$MgO_2 + H_2O \rightarrow Mg(OH)_2 + H_2O_2 \quad (4)$$

Solution pH has a significant impact on the degradation of organic

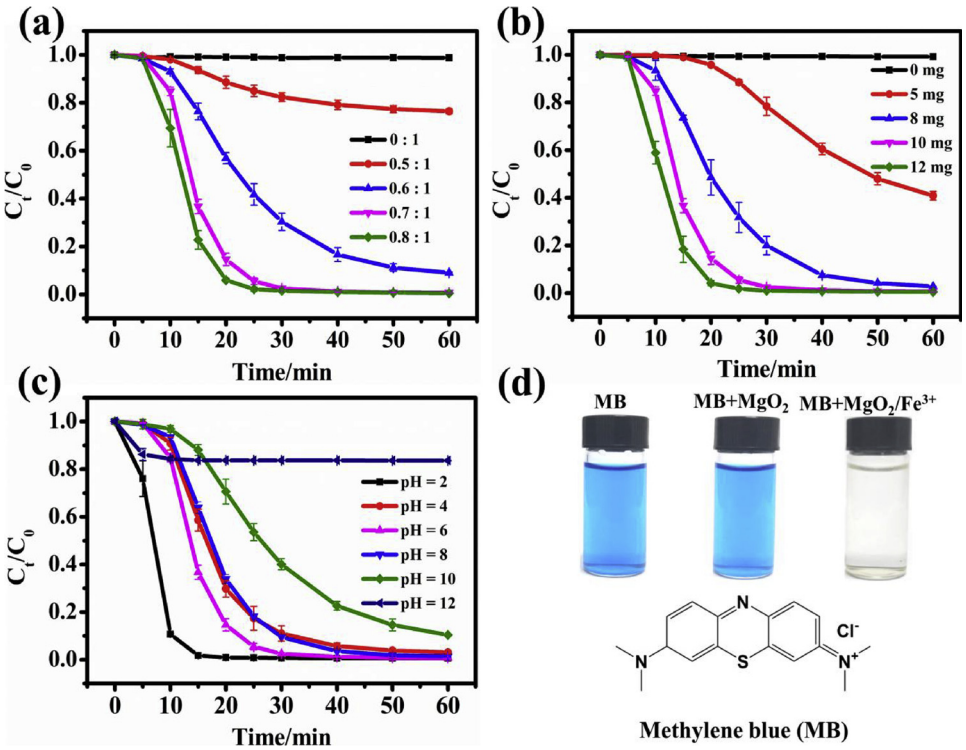

Fig. 3. Influences of the ratio of Fe^{3+} to MgO_2 (a), the dosage of MgO_2 (b), initial solution pH (c) on MB degradation in the MgO_2/Fe^{3+} system and color changes of MB solution (d).

dyes in Fenton/Fenton-like reactions. Hence, the oxidation degradation of MB in the MgO_2/Fe^{3+} system was evaluated at different initial solution pH from 2 to 12. From Fig. 3c, the MgO_2/Fe^{3+} system showed an excellent performance for MB degradation in the pH range of 2 -10. Even at a solution pH of 10, the removal rate of MB still reached up to 90% in 60 min. However, the degradation efficiency of MB was only 16.4% when the solution pH reached up to 12. Clearly, the degradation efficiency of MB increased with the decrease of initial pH except for pH 4. This is mainly attributed to the following three reasons: (i) the dissolution rate of MgO_2 and the yield of H_2O_2 increased with decreasing solution pH (Fig. S1c and S1d), (ii) the oxidation potential of ROS ($^{\cdot}OH$) would increase with a decrease of solution pH [37,38], and (iii) hydroxyl anions (OH^-) existed in a high-pH solution would compete with H_2O_2 for Fe^{3+} [39].

$$Fe^{3+} + 3OH^- = Fe(OH)_3\downarrow \quad (5)$$

3.3. Kinetics and mechanism of MB degradation

The kinetics of MB degradation in the MgO_2/Fe^{3+} system was investigated and the experimental data of MB degradation were fitted using pseudo-first-order kinetic and pseudo-second-order kinetic model [40,41], respectively. The fitting results of the experimental data for MB degradation under different conditions were shown in Fig. 4, and the corresponding regression coefficients (R^2) and kinetic rate constants obtained from these two kinetic models were listed in Table S1-S3. Comparing R^2 of the pseudo-first-order kinetic model with that of the pseudo-second-order kinetic model, it clearly indicated that the pseudo-first-order kinetic model is more applicable for explaining the degradation of MB in the MgO_2/Fe^{3+} system. As shown in Table S1–S3, an apparent increase in reaction rate constant with increasing the ratio of Fe^{3+} to MgO_2, the dosage of MgO_2 and decreasing solution pH apart from pH 4.

The temporal evolution of the UV–vis spectra of MB solution was investigated to analyze the process and mechanism of MB degradation. It was observed in Fig. 5a that the intensities of the two main adsorption peaks of MB at 291 nm and 664 nm gradually decreased with time. The peak located at 291 nm in the ultraviolet region was attributed to the $\pi \rightarrow \pi^*$ transition corresponding to unsaturated conjugate aromatic rings [42]. In the visible region, the adsorption peak appearing at 664 nm was ascribed to the chromophores functional groups of MB and its two dimers, namely −C═N, −C═S [43]. Here, the destruction of the conjugate structure in MB molecule was confirmed by the quick decay in the peak intensity of 664 nm. Moreover, the disappearance of the peak at 291 nm indirectly indicated that the aromatic fragments of MB and its intermediates were degraded. In addition to the decay of the peaks at 291 nm and 664 nm, it was noteworthy that a new weak absorbance peak at 788 nm appeared during the process of MB degradation. The intensity of the peak at 788 nm gradually increased in the first 10–15 minutes after the reaction started, then slowly decreased and finally disappeared in the following 15 min. This interesting phenomenon can confirm the formation and degradation of some intermediates during the process of MB degradation in the MgO_2/Fe^{3+} system.

For the degradation of organic dyes in water, the mineralization of organics also plays a significant role in the practical applications. The TOC of MB solution at different reaction time (0 min, 30 min, 24 h) was measured to evaluate the mineralization of MB. From Fig. 5b, 70.2% of TOC was removed within 30 min in the MgO_2/Fe^{3+} system. When the reaction time was prolonged to 24 h, the removal rate of TOC achieved up to 83.1%. The residual TOC in the reaction system may be attributed to the accumulation of some small molecular organic acids [44] from the degradation of MB. The results presented above indicated the as-prepared MgO_2 nanoparticles can efficiently degrade and mineralize MB in the presence of Fe^{3+}. More importantly, compared with previously reported oxidants (Table 2), a small amount of MgO_2 nanoparticles can rapidly degrade MB in solution.

As we all know, the degradation performance of Fenton/Fenton-like reactions is highly dependent on the generation of ROS in the degradation system. To identify the dominant ROS produced in the MgO_2/Fe^{3+} system, ESR spectroscopic experiments were performed using

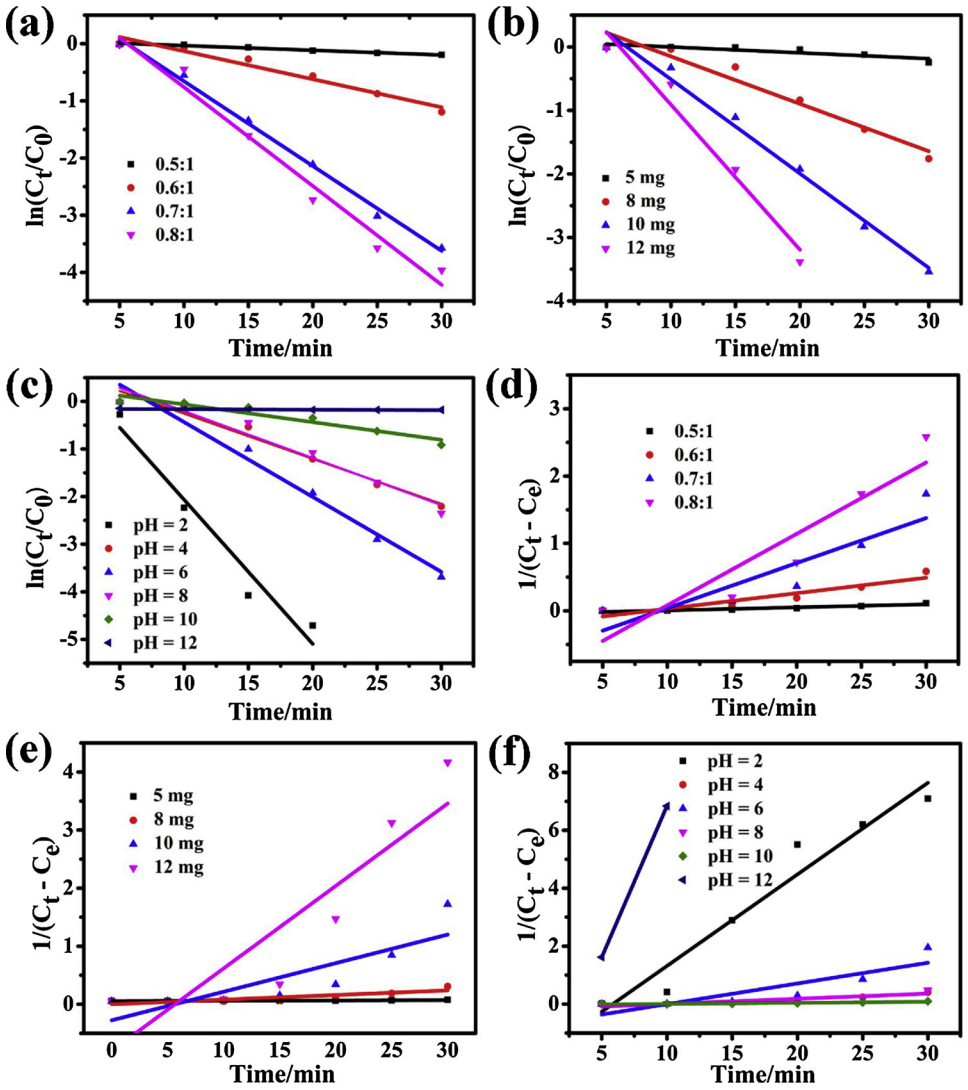

Fig. 4. Kinetic curves of MB degradation under different conditions: different molar ratio of Fe^{3+} to MgO_2 (a, d), different dosage of MgO_2 (b, e), different initial solution pH (c, f). (a–c fitted by Pseudo-first-order kinetic model; d–f fitted by pseudo-second-order kinetic model).

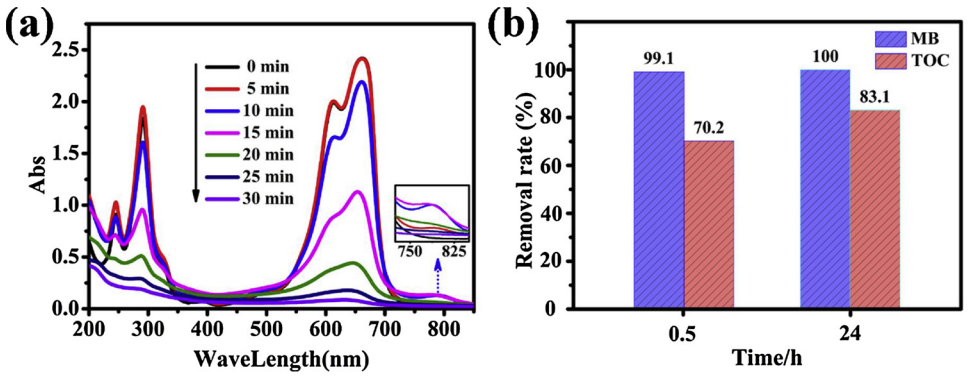

Fig. 5. Temporal evolution of the UV–vis spectra of MB degradation (a), removal rate of MB and TOC (b) in the MgO_2/Fe^{3+} system.

DMPO as a spin trapping agent. The resulting ESR spectra of MgO_2/Fe^{3+}–DMPO mixture and Fe^{3+}–DMPO mixture were described in Fig. 6a. The typical fourfold peaks consisted of a quartet with intensity ratios 1:2:2:1 with hyperfine coupling of $a_H = a_N = 1.49$ m T that appeared in the spectra of the MgO_2/Fe^{3+}–DMPO mixture, which was the characteristic signal of the DMPO–·OH adduct [51–54]. Moreover, the intensities of the quartet peaks became stronger with time. In contrast, the ESR spectrum of the Fe^{3+}–DMPO mixture showed a very weak signal of DMPO–·OH adduct, resulted from Fe^{3+} aqua complexes [55], which was not enough to trigger the degradation of MB. The above results corresponded with the MB degradation process in which none of the MB could be degraded without the MgO_2 nanoparticles (Fig. 3b), indicating the importance of MgO_2 nanoparticles in generating ·OH for MB degradation.

Table 2
Comparison of the performances of several reported oxidants for MB degradation.

Oxidant	Dosage of oxidant (mM)	Concentration of MB (mg/L)	pH	Degradation time (min)	Removal rate (%)	Reference
MgO_2	0.89	20	5.6	30	99.1	This work
CaO_2	13.9	3.2	–	90	90	[45]
H_2O_2	90	20	3	240	98	[46]
	40	100	5.4	30	< 80	[47]
	8.82	40	–	200	99	[48]
	352.9	10	–	180	73	[49]
$K_2S_2O_8$	5	4.8	6.4	60	> 90	[29]
$Na_2S_2O_8$	2.5	9.6	7	5	62.0	[50]

To further support the ·OH production during the degradation process of MB in the MgO_2/Fe^{3+} system, isopropanol (IP), as a hydroxyl radical scavenger [56–58], was added into the degradation reaction system (Fig. 6b). It can be seen that IP could significantly inhibit MB degradation in the MgO_2/Fe^{3+} system. As the concentration of IP increased, the inhibition of MB degradation became stronger. When the concentration of IP increased to 0.5 mM, almost no MB degradation was observed in the degradation reaction process. Evidently, the generated ·OH played a critical role in the degradation of MB [59,60]. Firstly, MgO_2 reacted slowly with H_2O to produce H_2O_2 (Eq. (4)), and then the decomposition of H_2O_2 catalyzed by Fe^{3+} gave strong oxidative ·OH to degrade organic dyes. Two other organic dyes, MG and MO, were adopted to evaluate the oxidation degradation ability of MgO_2 nanoparticles catalyzed by Fe^{3+}. As shown in Fig. S2, MgO_2 nanoparticles also exhibited enhanced degradation performance towards other types of organic dyes, suggesting a wide range of applications in the degradation of diverse organic dyes.

Interestingly, a small amount of black precipitate generated after the degradation of MB. To further investigate the components of the precipitate, the black residue was characterized by XRF and XRD. The XRF spectrum (Fig. 6c) showed the precipitate consisted of most Fe and a small amount of S and Mg elements, and the black precipitation in an amorphous form (Fig. S3) might result from the reaction and adsorption between Fe^{3+}/Fe^{2+} and the $Mg(OH)_2$ generated from MgO_2 via Eq. (4). It is noteworthy that the black precipitate still has cyclic catalytic performance for MB degradation in the presence of MgO_2 (Fig. 6d). As for the leakage of Mg^{2+} in the reaction system, the maximum concentration of Mg^{2+} in the reaction system was 21.33 mg/L even if all MgO_2 dissolved in aqueous solution without any precipitation, which was much lower than WHO and US EPA standards (50 mg/L) for drinking water [61]. As a result, the MgO_2/Fe^{3+} degradation system would not cause secondary pollution to water body, without further post-treatments.

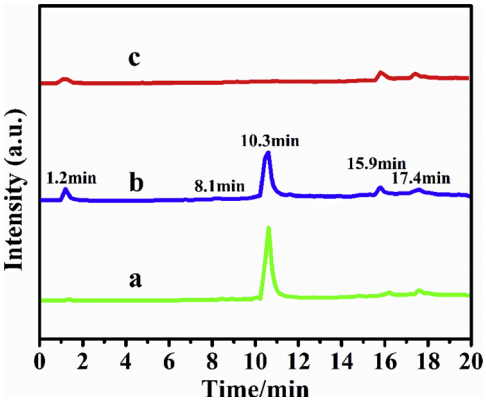

Fig. 7. HPLC spectra of MB solution after different reaction time (a: 0 min, b: 10 min, c: 30 min).

3.4. Possible pathways for MB degradation in the MgO_2/Fe^{3+} system

The identification of intermediates generated from the degradation of MB was conducted based on HPLC-MS technique in this study. The HPLC spectra of MB degradation (Fig. 7) showed that the intensity of the peak at 10.3 min representing MB dramatically declined compared with the spectrum of the initial MB solution after 10 min of degradation reaction performed, indicating the degradation of MB. In addition, the relative intensity of three peaks at 1.2, 15.6 and 17.4 min obviously increased as time went on, further confirmed the degradation of MB and

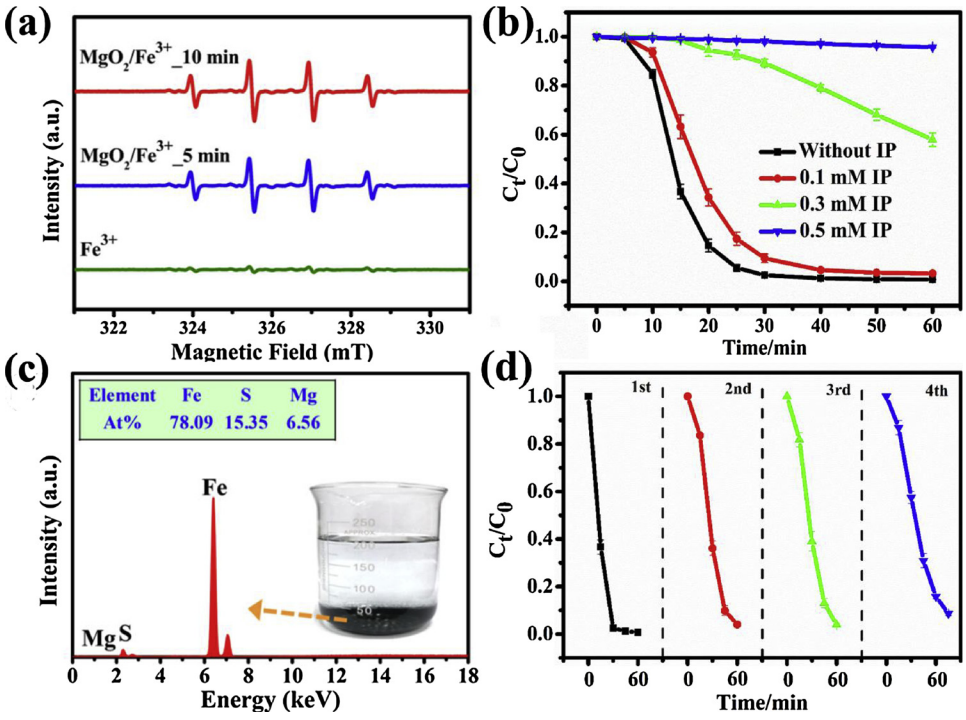

Fig. 6. ESR spectra for detecting DMPO–·OH in Fe^{3+} and MgO_2/Fe^{3+} system (a), MB degradation with addition of different amounts of isopropanol (IP) (b), XRF spectrum of the black residue after the degradation reaction (c), the cyclic catalytic performance of the black residue towards MB degradation (d). Conditions: 200 mL of MB solution (20 mg/L), 10 mg of MgO_2, 25 mg of $Fe_2(SO_4)_3xH_2O$.

the formation of intermediates. Moreover, when the reaction time prolonged to 30 min, the peak at 10.3 min disappeared, suggesting the complete destruction of MB molecular. The result above revealed the degradation of MB and the formation of intermediates in the MgO_2/Fe^{3+} system, which was in consistent with the result of UV–vis spectra of MB degradation.

The ESI-MS spectra recorded for original MB solution and 10 min-degraded MB solution at different retention times were presented in Fig. S4. From the MS spectrum of original MB solution (Fig. S4a), the signals at m/z = 284 and 270 were ascribed to MB and its demethylation form, respectively [62,63]. As for the 10 min-degraded solution, the MS spectrum of intermediates at the retention time of 17.4 min (Fig. S4e) displayed the signals at m/z = 301 and 318, which can be assigned to the hydroxylation of MB [64]. At the retention time of 8.1 min (Fig. S4c), the MS peaks at m/z = 302, 318, 336 and 350 were attributed to the formation of sulfoxide and following consecutive hydroxylation [65]. In addition, the relative intensity of the signal at m/z = 270 from the demethylated MB became stronger than that of original MB solution (Fig. S4d), indicating the demethylation of MB was improved in the MgO_2/Fe^{3+} degradation system [66,67]. Here, it could be generalized that the degradation process of MB occurred via three parallel reaction pathways: (i) N-demethylation of MB, (ii) direct hydroxylation of MB by ·OH radicals and (iii) sulfoxidation of MB and subsequent hydroxylation. Further, the fragment peaks at low m/z = 69, 87, 201, 219, 233 were observed in the MS spectrum at the retention time of 1.2 min (Fig. S4b), which resulted from the opening of central aromatic-like ring and two side aromatic rings of MB molecule [63,65,68–71]. The appearance of low-molecular peaks confirmed successful breaking up of MB structure into smaller fragments. Based on the discussion and analysis above, the proposed pathways for MB degradation in the MgO_2/Fe^{3+} system were presented in Fig. 8.

4. Conclusion

In summary, highly pure MgO_2 nanoparticles (94.26 wt%) were successfully synthesized and used as a Fenton-like oxidant to degrade and mineralize organic dyes in this work. A small amount of as-obtained MgO_2 nanoparticles could effectively degrade diverse organic dyes, indicating that MgO_2 nanoparticles are an efficient Fenton-like oxidant for enhanced dye degradation. The generation of ·OH in the MgO_2/Fe^{3+} system was considered to be responsible for efficient degradation performance towards organic dyes. The procedure of organics degradation in the MgO_2/Fe^{3+} system can be conducted in a wide range of pH (2–10) at room temperature. Furthermore, three possible pathways of MB degradation were proposed according to the HPLC-MS analysis of degradation intermediates. Taking account of cost-effectiveness, environmental friendliness, and easy preparation, as well as a wide range of applications, MgO_2 nanoparticles would be a promising oxidant for Fenton-like reactions in remedying organic-polluted water even soil.

Acknowledgments

The authors acknowledge the experimental help from Huazhong University of Science & Technology Analytical and Testing Center. X. Wang was supported by the National Science Foundation for Distinguished Young Scholars of China (No. 51725504). P.K. Wong was supported by CAS/SAFEA International Partnership Program for Creative Research Teams of Chinese Academy of Sciences (2015HSC-UE004).

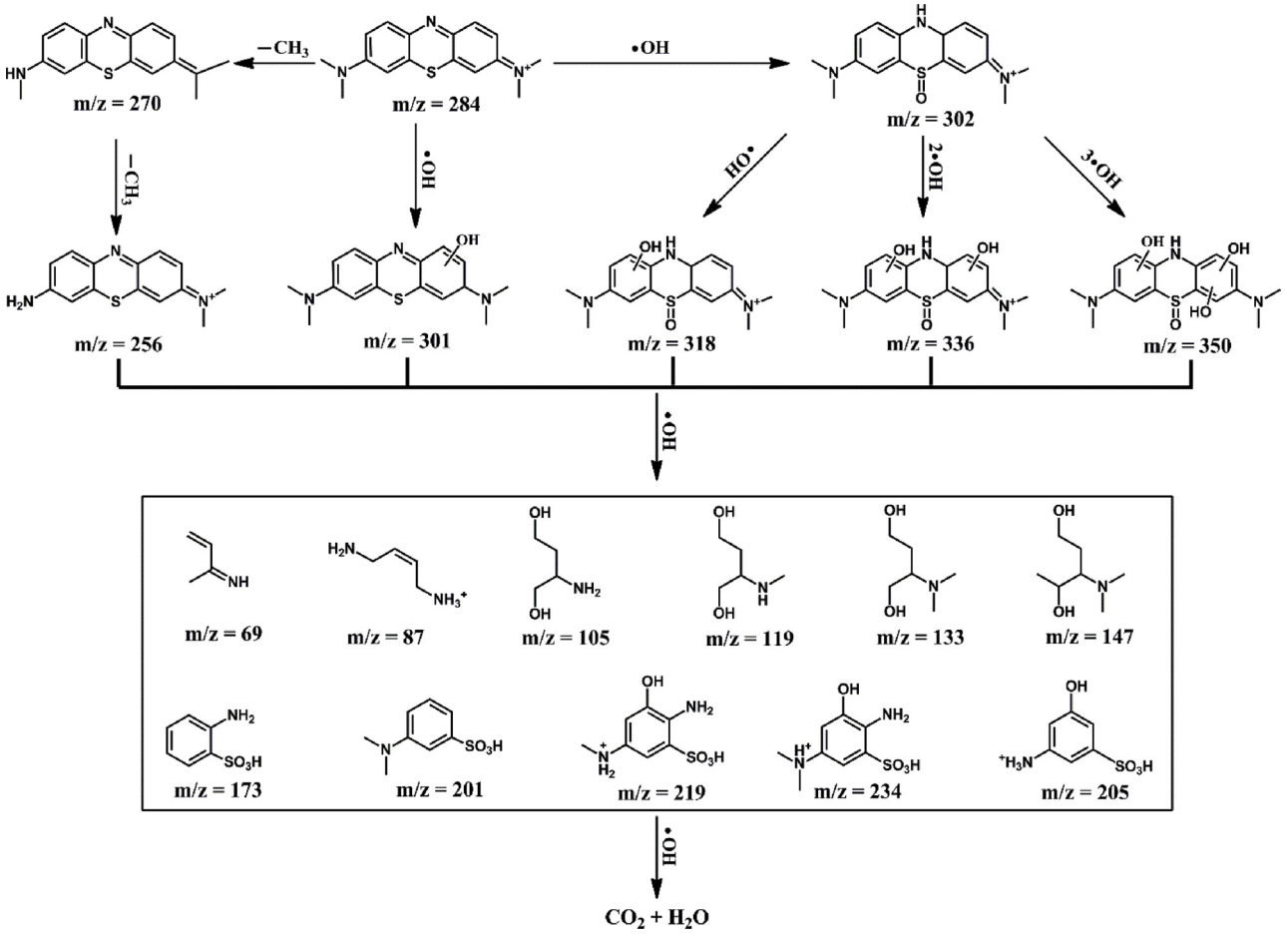

Fig. 8. Proposed pathways for MB degradation in the MgO_2/Fe^{3+} system.

Appendix A. Supplementary data

Supplementary material related to this article can be found, in the online version, at doi:https://doi.org/10.1016/j.jhazmat.2019.04.058.

References

[1] F.C. Moreira, R.A. Boaventura, E. Brillas, V.J. Vilar, Electrochemical advanced oxidation processes: a review on their application to synthetic and real wastewaters, Appl. Catal. B: Environ. 202 (2017) 217–261.

[2] D.B. Miklos, C. Remy, M. Jekel, K.G. Linden, J.E. Drewes, U. Hübner, Evaluation of advanced oxidation processes for water and wastewater treatment–a critical review, Water Res. 139 (2018) 118–131.

[3] Y.-H. Chuang, S. Chen, C.J. Chinn, W.A. Mitch, Comparing the UV/monochloramine and UV/free chlorine advanced oxidation processes (AOPs) to the UV/hydrogen peroxide AOP under scenarios relevant to potable reuse, Environ. Sci. Technol. 51 (2017) 13859–13868.

[4] N.E. Thornburg, S.L. Nauert, A.B. Thompson, J.M. Notestein, Synthesis − structure–function relationships of silica-supported niobium(V) catalysts for alkene epoxidation with H_2O_2, ACS Catal. 6 (2016) 6124–6134.

[5] Z. Tang, Y. Liu, M. He, W. Bu, Chemodynamic therapy: tumour microenvironment-mediated Fenton and Fenton-like reactions, Angew. Chem. Int. Ed. 57 (2018) 2–13.

[6] X. Qian, M. Ren, Y. Zhu, D. Yue, Y. Han, J. Jia, Y. Zhao, Visible light assisted heterogeneous Fenton-like degradation of organic pollutant via α-FeOOH/mesoporous carbon composites, Environ.Sci. Technol. 51 (2017) 3993–4000.

[7] J. Ma, L. Xu, C. Shen, C. Hu, W. Liu, Y. Wen, Fe-N-graphene wrapped Al_2O_3/pentlandite from microalgae: high Fenton catalytic efficiency from enhanced Fe^{3+} reduction, Environ.Sci. Technol. 52 (2018) 3608–3614.

[8] N. Jiang, L. Lyu, G. Yu, L. Zhang, C. Hu, A dual-reaction-center Fenton-like process on –C≡N–Cu linkage between copper oxides and defect-containing g-C_3N_4 for efficient removal of organic pollutants, J. Mater. Chem. A 6 (2018) 17819–17828.

[9] Y. Zhou, X. Fang, T. Wang, Y. Hu, J. Lu, Chelating agents enhanced CaO_2 oxidation of bisphenol A catalyzed by Fe^{3+} and reuse of ferric sludge as a source of catalyst, Chem. Eng. J. 313 (2017) 638–645.

[10] D.M. White, R.L. Irvine, C.R. Woolard, The use of solid peroxides to stimulate growth of aerobic microbes in tundra, J. Hazard. Mater. 57 (1998) 71–78.

[11] https://monographs.iarc.fr/list-of-classifications-volumes/.

[12] Y. Weng, Z. Weng, Z. Liang, H. Lyu, Z. Zhuang, Y. Yu, Mesoporous Ca–Mn–O as an efficient scavenger toward organic pollutants and heavy metals: ion exchange provoking ultrafast Fenton-like reaction based on the synergy of alkaline earth/transition metals, J. Mater. Chem. A 6 (2018) 9528–9538.

[13] D.A. Giannakoudakis, M. Florent, R. Wallace, J. Secor, C. Karwacki, T.J. Bandosz, Zinc peroxide nanoparticles: surface, chemical and optical properties and the effect of thermal treatment on the detoxification of mustard gas, Appl. Catal. B: Environ. 226 (2018) 429–440.

[14] B.-C. Huang, J. Jiang, G.-X. Huang, H.-Q. Yu, Sludge biochar-based catalysts for improved pollutant degradation by activating peroxymonosulfate, J. Mater. Chem. A 6 (2018) 8978–8985.

[15] X. Li, Z. Ao, J. Liu, H. Sun, A.I. Rykov, J. Wang, Topotactic transformation of metal–organic frameworks to graphene-encapsulated transition-metal nitrides as efficient Fenton-like catalysts, ACS Nano 10 (2016) 11532–11540.

[16] G. Zhang, Z. Wu, H. Liu, Q. Ji, J. Qu, J. Li, Photoactuation healing of α-FeOOH@g-C_3N_4 catalyst for efficient and stable activation of persulfate, Small 13 (2017) 1702225-1701132.

[17] M. Viisimaa, O. Karpenko, V. Novikov, M. Trapido, A. Goi, Influence of biosurfactant on combined chemical–biological treatment of PCB-contaminated soil, Chem. Eng. J. 220 (2013) 352–359.

[18] V.L. Prasanna, R. Vijayaraghavan, Simultaneous Fenton–photocatalytic reactions through a new single catalyst (nano ZnO_2 /Fe^{2+}) for dye degradation, J. Phys. Chem. C 121 (2017) 18557–18563.

[19] C.P. Gerba, K. Hou, M.D. Sobsey, Microbial removal and inactivation from water by filters containing magnesium peroxide, J. Environ. Sci. Heal. A 23 (2008) 41–58.

[20] J. Jaison, C. Ashok raja, S. Balakumar, Y.S. Chan, Sol-Gel synthesis and characterization of magnesium peroxide nanoparticles, IOP Conf. Ser. Mater. Sci. Eng. 78 (2015) 012005.

[21] J.M. Burlitch, M.L. Beeman, B. Riley, D.L. Kohlstedt, Low-temperature syntheses of olivine and forsterite facilitated by hydrogen peroxide, Chem. Mater. 3 (1991) 692–698.

[22] A. Goi, M. Viisimaa, M. Trapido, R. Munter, Polychlorinated biphenyls-containing electrical insulating oil contaminated soil treatment with calcium and magnesium peroxides, Chemosphere 82 (2011) 1196–1201.

[23] Y.-J. Chang, Y.-T. Chang, C.-H. Hung, The use of magnesium peroxide for the inhibition of sulfate-reducing bacteria under anoxic conditions, J. Ind. Microbiol. Biotechnol. 35 (2008) 1481–1491.

[24] Y. Wolanov, P.V. Prikhodchenko, A.G. Medvedev, R. Pedahzur, O. Lev, Zinc dioxide nanoparticulates: a hydrogen peroxide source at moderate pH, Environ. Sci. Technol. 47 (2013) 8769–8774.

[25] Amina, X. Si, K. Wu, Y. Si, B. Yousaf, Synergistic effects and mechanisms of hydroxyl radical-mediated oxidative degradation of sulfamethoxazole by Fe(II)-EDTA catalyzed calcium peroxide: Implications for remediation of antibiotic-contaminated water, Chem. Eng. J. 353 (2018) 80–91.

[26] D.A. Giannakoudakis, M. Florent, R. Wallace, J. Secor, C. Karwacki, T.J. Bandosz, Zinc peroxide nanoparticles: Surface, chemical and optical properties and the effect of thermal treatment on the detoxification of mustard gas, Appl. Catal. B: Environ. 226 (226) (2018) 429–440.

[27] A.J. Carrillo, D. Sastre, D.P. Serrano, P. Pizarro, J.M. Coronado, Revisiting the BaO_2/BaO redox cycle for solar thermochemical energy storage, Phys. Chem. Chem. Phys. 18 (2016) 8039–8048.

[28] S. Gao, M. Wang, Y. Chen, M. Tian, Y. Zhu, X. Wei, T. Jiang, An advanced electro-Fenton degradation system with triboelectric nanogenerator as electric supply and biomass-derived carbon materials as cathode catalyst, Nano Energy 45 (45) (2018) 21–27.

[29] D. Ding, C. Liu, Y. Ji, Q. Yang, L. Chen, C. Jiang, T. Cai, Mechanism insight of degradation of norfloxacin by magnetite nanoparticles activated persulfate: identification of radicals and degradation pathway, Chem. Eng. J. 308 (2017) 330–339.

[30] G. Fang, W. Wu, C. Liu, D.D. Dionysiou, Y. Deng, D. Zhou, Activation of persulfate with vanadium species for PCBs degradation: a mechanistic study, Appl. Catal. B: Environ. 202 (2017) 1–11.

[31] Y. Zhao, B. Yuan, Z. Zheng, R. Hao, Removal of multi-pollutant from flue gas utilizing ammonium persulfate solution catalyzed by Fe/ZSM-5, J. Hazard. Mater. 362 (2018) 266–274.

[32] M. Danish, X. Gu, S. Lu, A. Ahmad, M. Naqvi, U. Farooq, X. Zhang, X. Fu, Z. Miao, Y. Xue, Efficient transformation of trichloroethylene activated through sodium percarbonate using heterogeneous zeolite supported nano zero valent iron-copper bimetallic composite, Chem. Eng. J. 308 (2016) 396–407.

[33] X. Zheng, M. Huang, Y. You, X. Fu, Y. Liu, J. Wen, One-pot synthesis of sandwich-like MgO@Carbon with enhanced sorption capacity of organic dye, Chem. Eng. J. 334 (2018) 1399–1409.

[34] A.A. Rywak, J.M. Burlitch, T.M. Loehr, Sol-gel preparation and characterization of magnesium peroxide, magnesium hydroxide methoxide, and randomly and (111) oriented MgO thin films, Chem. Mater. 7 (1995) 2028–2038.

[35] X. Jiang, S. Li, L. Shao, Pushing CO_2-philic membrane performance to the limit by designing semi-interpenetrating networks (SIPN) for sustainable CO_2 separations, Environ. Eng. Sci. 10 (2017) 1339–1344.

[36] W. Ma, X. Liu, C. Li, H. Yin, W. Xi, R. Liu, G. He, X. Zhao, J. Luo, Y. Ding, Rechargeable Al-CO_2 batteries for reversible utilization of CO_2, Adv. Mater. 30 (2018) 1801152.

[37] B.G. Kwon, S.L. Dong, N. Kang, J. Yoon, Characteristics of p-chlorophenol oxidation by Fenton's reagent, Water Res. 33 (1999) 2110–2118.

[38] R. Thiruvenkatachari, T.O. Kwon, J.C. Jun, S. Balaji, M. Matheswaran, I.S. Moon, Application of several advanced oxidation processes for the destruction of terephthalic acid (TPA), J. Hazard. Mater. 142 (2007) 308–314.

[39] G. Subramanian, G. Madras, Remarkable enhancement of Fenton degradation at a wide pH range promoted by thioglycolic acid, Chem. Commun. 53 (2017) 1136–1139.

[40] K.Y. Cho, Y.S. Yeom, H.Y. Seo, P. Kumar, A.S. Lee, K.-Y. Baek, H.G. Yoon, Ionic block copolymer doped reduced graphene oxide supports with ultra-fine Pd nanoparticles: strategic realization of ultra-accelerated nanocatalysis, J. Mater. Chem. A 3 (2015) 20471–20476.

[41] Z. Bao, L. Ye, B. Fang, L. Zhao, Synthesis of $Fe_{0.32}Co_{0.68}$/γ-Al_2O_3@C nanocomposite for depth treatment of dye sewage based on adsorption and advanced catalytic oxidation, J. Mater. Chem. A 5 (2017) 6664–6676.

[42] Y. Li, F.-S. Zhang, Catalytic oxidation of methyl orange by an amorphous FeOOH catalyst developed from a high iron-containing fly ash, Chem. Eng. J. 158 (2010) 148–153.

[43] B. Zhou, X. Zhao, H. Liu, J. Qu, C.P. Huang, Visible-light sensitive cobalt-doped $BiVO_4$ (Co-$BiVO_4$) photocatalytic composites for the degradation of methylene blue dye in dilute aqueous solutions, Appl. Catal. B: Environ. 99 (2010) 214–221.

[44] S. Zhang, Q. Fan, H. Gao, Y. Huang, X. Liu, J. Li, X. Xu, X. Wang, Formation of Fe_3O_4@MnO_2 ball-in-ball hollow spheres as a high performance catalyst with enhanced catalytic performances, J. Mater. Chem. A 4 (2016) 1414–1422.

[45] P. Kaewdee, N. Chandet, G. Rujijanagul, C. Randorn, Multicatalytic properties of nanoparticle CaO_2 synthesized by a novel, simple and economical method for wastewater treatment, Catal. Commun. 84 (2016) 151–154.

[46] Y. He, B. Jiang, Y. Jiang, J. Chen, Y.X. Zhang, Evaluation of MnO_2-templated iron oxide-coated diatomites for their catalytic performance in heterogeneous photo Fenton-like system, J. Hazard. Mater. 344 (2018) 230–240.

[47] S.H. Yoo, D. Jang, H.-I. Joh, S. Lee, Iron oxide/porous carbon as a heterogeneous Fenton catalyst for fast decomposition of hydrogen peroxide and efficient removal of methylene blue, J. Mater. Chem. A 5 (2017) 748–755.

[48] C.-F. Zhang, L.-G. Qiu, F. Ke, Y.-J. Zhu, Y.-P. Yuan, G.-S. Xu, X. Jiang, A novel magnetic recyclable photocatalyst based on a core–shell metal–organic framework Fe_3O_4@MIL-100(Fe) for the decolorization of methylene blue dye, J. Mater. Chem. A 1 (2013) 14329–14334.

[49] Y. Wang, L. Zhu, X. Yang, E. Shao, X. Deng, N. Liu, M. Wu, Facile synthesis of three-dimensional $Mn3O_4$ hierarchical microstructures and their application in the degradation of methylene blue, J. Mater. Chem. A 3 (2015) 2934–2941.

[50] Y.-H. Jo, S.-H. Hong, T.-J. Park, S.-H. Do, The synthesized and thermally modified Mn–Ca–FeOOH composite in persulfate system: its role to discolor methylene blue, Appl. Surf. Sci. 301 (2014) 576–583.

[51] G.R. Buettner, Spin trapping: ESR parameters of spin adducts, Free Radic. Biol. Med. 3 (1987) 259–303.

[52] G. Fang, J. Gao, D.D. Dionysiou, C. Liu, D. Zhou, Activation of persulfate by quinones: free radical reactions and implication for the degradation of PCBs, Environ.Sci. Technol. 47 (2013) 4605–4611.

[53] Y. Liu, Q. Wang, Removal of elemental mercury from flue gas by thermally activated ammonium persulfate in a bubble column reactor, Environ.Sci. Technol. 48 (2014) 12181–12189.

[54] H. Gao, H. Yang, J. Xu, S. Zhang, J. Li, Strongly coupled g-C_3N_4 nanosheets-Co_3O_4

quantum dots as 2D/0D heterostructure composite for peroxymonosulfate activation, Small (2018) 1801353.
[55] V.A. Timoshnikov, T.V. Kobzeva, N.E. Polyakov, G.J. Kontoghiorghes, Inhibition of Fe^{2+}- and Fe^{3+}- induced hydroxyl radical production by the iron-chelating drug deferiprone, Free Radic. Biol. Med. 78 (2015) 118–122.
[56] B.C. Ma, S. Ghasimi, K. Landfester, F. Vilela, K.A.I. Zhang, Conjugated microporous polymer nanoparticles with enhanced dispersibility and water compatibility for photocatalytic applications, J. Mater. Chem. A 3 (2015) 16064–16071.
[57] Q. Zhang, P. Chen, M. Zhuo, F. Wang, Y. Su, T. Chen, K. Yao, Z. Cai, W. Lv, G. Liu, Degradation of indometacin by simulated sunlight activated CDs-loaded $BiPO_4$ photocatalyst: roles of oxidative species, Appl. Catal. B: Environ. 221 (2018) 129–139.
[58] L. Ge, Z. Peng, W. Wang, F. Tan, X. Wang, B. Su, X. Qiao, P.K. Wong, g-C_3N_4/MgO nanosheets: light-independent, metal-poisoning-free catalysts for the activation of hydrogen peroxide to degrade organics, J. Mater. Chem. A 6 (2018) 16421–16429.
[59] J. Ding, Q. Zhong, S. Zhang, F. Song, Y. Bu, Simultaneous removal of NOX and SO_2 from coal-fired flue gas by catalytic oxidation-removal process with H_2O_2, Chem. Eng. J. 243 (2014) 176–182.
[60] A.L. Pham, C. Lee, F.M. Doyle, D.L. Sedlak, A silica-supported iron oxide catalyst capable of activating hydrogen peroxide at neutral pH values, Environ. Sci. Technol. 43 (2009) 8930–8935.
[61] M.P. Thomas, Calcium and magnesium in drinking-water: public health significance, Perspect. Public Health 130 (2009) 612–613.
[62] D. Wiedmer, E. Sagstuen, K. Welch, H.J. Haugen, H. Tiainen, Oxidative power of aqueous non-irradiated TiO_2-H_2O_2 suspensions: methylene blue degradation and the role of reactive oxygen species, Appl. Catal. B: Environ. 198 (2016) 9–15.
[63] H.W. Carvalho, A.P.L. Batista, P. Hammer, T.C. Ramalho, Photocatalytic degradation of methylene blue by TiO_2-Cu thin films: theoretical and experimental study, J. Hazard. Mater. 184 (2010) 273–280.
[64] L.C.A. Oliveira, M. Gonçalves, M.C. Guerreiro, T.C. Ramalho, J.D. Fabris, M.C. Pereira, K. Sapag, A new catalyst material based on niobia/iron oxide composite on the oxidation of organic contaminants in water via heterogeneous Fenton mechanisms, Appl. Catal. A: Gen. 316 (2007) 117–124.
[65] A. Houas, H. Lachheb, M. Ksibi, E. Elaloui, C. Guillard, J.M. Herrmann, Photocatalytic degradation pathway of methylene blue in water, Appl. Catal. B: Environ. 31 (2001) 145–157.
[66] H.S. Oliveira, L.C.A. Oliveira, M.C. Pereira, J.D. Ardisson, P.P. Souza, P.O. Patrício, F.C.C. Moura, Nanostructured vanadium-doped iron oxide: catalytic oxidation of methylene blue dye, New J. Chem. 39 (2015) 3051–3058.
[67] H.S. Oliveira, L.D. Almeida, V.A.A.de Freitas, F.C.C. Moura, P.P. Souza, L.C.A. Oliveira, Nb-doped hematite: highly active catalyst for the oxidation of organic dyes in water, Catal. Today 240 (2015) 176–181.
[68] J. Lin, R. Zong, M. Zhou, Y. Zhu, Photoelectric catalytic degradation of methylene blue by C60-modified TiO_2 nanotube array, Appl. Catal. B: Environ. 89 (2009) 425–431.
[69] L.V. Trandafilović, D.J. Jovanović, X. Zhang, S. Ptasińska, M.D. Dramićanin, Enhanced photocatalytic degradation of methylene blue and methyl orange by ZnO:Eu nanoparticles, Appl. Catal. B: Environ. 203 (2017) 740–752.
[70] M.A. Rauf, M.A. Meetani, A. Khaleel, A. Ahmed, Photocatalytic degradation of Methylene Blue using a mixed catalyst and product analysis by LC/MS, Chem. Eng. J. 157 (2010) 373–378.
[71] H.W.P. Carvalho, A.P.L. Batista, P. Hammer, T.C. Ramalho, Photocatalytic degradation of methylene blue by TiO_2-Cu thin films: theoretical and experimental study, J. Hazard. Mater. 184 (2010) 273–280.